ANALYSIS OF WAKES INTERACTIONS IN A HIGH-SPEED LOW-PRESSURE TURBINE CASCADE USING LARGE-EDDY SIMULATIONS

A. Boudin[1] *- J. Dombard*[1] *- F. Duchaine*[1] *- L. Gicquel*[1] *- N. Odier*[1] *-*
S. Lavagnoli[2] *- G. Lopes*[2] *- L. Simonassi*[2] *- C. Uribe*[3]

[1]Computational Fluid Dynamics, CERFACS, Toulouse, France, boudin@cerfacs.fr - dombard@cerfacs.fr - duchaine@cerfacs.fr - gicquel@cerfacs.fr - odier@cerfacs.fr
[2]Turbomachinery and Propulsion, Von Karman Institute, Rhode-Saint-Genèse, Belgium, sergio.lavagnoli@vki.ac.be - gustavo.lopes@vki.ac.be - loris.simonassi@vki.ac.be
[3]BE module TuBP, Safran Aircraft Engines, Moissy-Cramayel, France, cedric.uribe@safrangroup.com

ABSTRACT

Turbomachinery flows are highly turbulent and prone to different types of instabilities. In low-pressure turbines (LPT), the wakes from the upstream bladerows provide the dominant source of unsteadiness. For Reynolds numbers at which LPT are generally operating, the majority of the blade boundary layer remains laminar. As a matter of fact, the suction side boundary layer of such flow is responsible for most of the efficiency loss. It is thus crucial to master the impact of the incoming wake turbulence and its effect on the transition of this boundary layer to master the generated losses. Such a rotor/stator interaction in new generation of low-pressure turbines, with the particularity of being locally transonic, is addressed numerically in this work. The considered geometry consists in a linear blade cascade in front of which bars rotate, acting as wake generators that periodically impact the blades leading edges, thereby influencing the aerodynamics of the cascade. For this study, Large-Eddy Simulations (LES) are carried out and compared to experimental results acquired at the Von Karman Institute during the Cleansky project SPLEEN. This paper investigates the interactions between the periodically incoming wakes and the turbine cascade. The transition of the suction side boundary layer, the pressure side separation bubble and the wall shear stress on the blade surface are specifically analysed along with the temporal evolution of the sonic pocket.

KEYWORDS

LARGE-EDDY SIMULATION, HIGH-SPEED LOW-PRESSURE TURBINE, ROTOR/STATOR INTERACTION

NOMENCLATURE

c	chord length
E	total energy
g	pitch
L_i	integral length scale
M	Mach number
M_{is}	isentropic Mach number
P	hydrostatic pressure
P_t	total pressure

Abbreviations

CFL	Courant-Friedrichs-Lewy
CPU	Central Processing Unit
DNS	Direct Numerical Simulation
FST	Free-Stream Turbulence
LE	Leading Edge
LES	Large-Eddy Simulation
LPT	Low-Pressure Turbine
SGS	Subgrid Scale

q_j	heat flux vector
q_j^t	SGS heat flux vector
R	gas constant
Re_{is}	isentropic Reynolds number
t	time
T_t	total temperature
Tu	turbulence intensity
u_i	velocity vector
x^+, y^+, z^+	dimensionless cell sizes
$\Delta x, \Delta y, \Delta z$	cell sizes

TE	Trailing Edge
TKE	Turbulent Kinetic Energy
WALE	Wall-Adapting Local Eddy viscosity

Greek

α	aspect ratio
α_{in}	incidence at the inlet
δ_{ij}	Kronecker delta
γ	Laplace coefficient
ρ	density
τ_{ij}	laminar stress tensor
τ_{ij}^t	Reynolds tensor

INTRODUCTION

The low-pressure turbine (LPT) may represent up to 30% of the total jet engine weight, although its dimension is itself limited by the engine diameter. Reducing its number of blades is hence desired to limit its weight while lowering its cost of operation. However, reducing the number of blades is not straightforward. It implies that remaining blades need to generate more lift while experiencing higher loading. Classical LPT generally operates at Reynolds numbers ranging from 0.5×10^5 to 5.0×10^5. At this range of Reynolds numbers, boundary layer transition and separation have to be finely controlled and simulations need to take these aspects into consideration to correctly predict the turbine performance (Hodson and Howell, 2005a). Medic and Sharma (2012) showed in this context that Large-Eddy Simulations (LES) of a LPT cascade at different Reynolds numbers and different levels of free-stream turbulence (FST) capture, on the suction side, the appearance of a separation point as well as a reattachment point while correctly evaluating the total pressure losses. It is also known that such a flow is strongly influenced by unsteady interactions with the previous or next stages. One of the major mechanisms occurring in that case is the influence of the wakes shed at the trailing edge of the blades from the upstream row. Hodson and Howell (2005b) explained how these wakes impact the transition process of attached or separated flows. Many authors have since measured the impact of periodically incoming wakes on the boundary layer development of ultra-high-lift LPT airfoils, either experimentally (Lu et al., 2017) or numerically. Bechlars et al. (2016), for example, highlighted the coupling mechanism between the upstream turbulence, the separation bubble and the trailing edge, in particular the Kelvin-Helmholtz instabilities, on a T106A low-pressure turbine blade by use of Direct Numerical Simulations (DNS). Bolinches-Gisbert et al. (2021) compared experimental to numerical data and showed the influence of the reduced frequency of the wakes on the separation bubble length present on the suction side as well as the total pressure losses of such blades. Other papers (Michelassi et al., 2003a, 2015) present results of LES and DNS for the T106 linear cascade with bars acting as wake generators. Michelassi et al. (2003b) typically compared results obtained from DNS, LES and URANS for similar configurations.

As detailed above, many authors already studied wake effect on LPT blades demonstrating its impact on the transition of the boundary layers and on the overall pressure losses. However the need for increase of efficiency brought new technologies accompanied by new challenges. For example, "high-speed" low pressure turbines are concepts investigated for future LPT generations within the European project SPLEEN. These indeed allow to reduce the number of stages while keeping the same output power, leading to weight and space reduction. Such low

pressure turbines however have a higher rotation rate meaning that the flow velocity seen by the blades is much higher than for classical LPT. As a result, a locally transonic flow regime is present in the vein, and consequently a new aerodynamics occurs compared to current geometries. With this new context, the main objective of the present paper is to evaluate the ability of Large Eddy Simulations to serve as an investigation tool and to conduct a first numerical study of the effect of bars, acting as wake generators, in such conditions. To do so, an incremental comparison is done, starting with an isolated vane simulation and then adding the upstream rotating bars, simulating the complete experimental setup. In particular the influence of the configuration on the flow turbulence is investigated and its impact on the blade loading and the behaviour of the boundary layers is detailed. Finally, a brief discussion is made about the mean pressure losses.

TEST CASE DESCRIPTION

The configuration studied numerically is based on a test bench configuration located at the Von Karman Institute developed within the project SPLEEN (Simonassi et al., 2022). It is composed of a linear cascade of high-speed low-pressure turbine blades in front of which moving bars of cylinder shape are placed. The bars are all aligned with the blades cascade at a given distance and with a pitchwise distance that is the same as the one of the blades (32.95 mm), noted (g) on Figure 1. This means that the bar-to-blade ratio is 1, which greatly simplifies the simulations by allowing to consider only a small section of the entire cascade. The diameter of the bars is 1 millimeter and the chord length of the blades, noted (c) on Figure 1, is 52.28 millimeters. The pitch-to-chord ratio of the blades is 0.63, the theoretical inlet angle is $37.3°$ and the theoretical outlet angle is $53.8°$. Finally, the distance between the bars and the blades leading edges is roughly one chord length (53.57 mm). For this study, the bars are moving downward at a translation velocity of 165 meters per second.

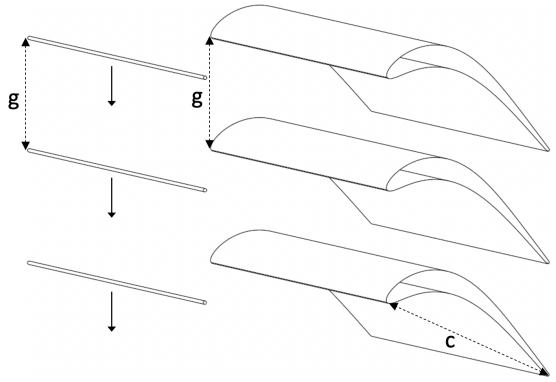

Figure 1: Configuration of the linear blades cascade with the upstream moving bars.

Two test cases are considered in the following. The first one (denoted case A) has no bar and the blades are operating at nominal conditions. The second one (denoted case B) includes the upstream moving bars and is used to evaluate their impact on the flow and the cascade performance. Note that only the center section of the actual configuration is investigated, and the end-walls are not considered in the simulations.

NUMERICAL APPROACH AND MODELING

In terms of approach, and as the end-walls are not taken into account, only a central slice of the cascade is computed. A couple of two blades and two bars is considered and periodicity is applied in the spanwise and pitchwise directions to emulate the real test bench. When considering the case with moving bars, two domains are created (one for each part) and a coupling method is used to transfer the information at the interface between the moving domain attached to the bars and the static one attached to the blades. The AVBP code (Schonfeld and Rudgyard, 1999) developed at CERFACS is used to tackle this specific problem by use of the MISCOG approach (Wang et al., 2014, de Laborderie et al., 2018). AVBP is a massively parallel code that solves the compressible Navier-Stokes equations on unstructured hybrid meshes. It is dedicated to unsteady compressible flows in complex geometries with or without combustion and is thus very suitable for turbomachinery flows (Dombard et al., 2020, de Laborderie et al., 2020). In the following, wall-resolved LES are produced to finely capture the flow behaviour near walls and capture features such as boundary layer separation, transition, etc (Segui et al., 2017, Dupuy et al., 2020).

In terms of numerics, the convective part of the Navier-Stokes equations is solved using a two-step time explicit Taylor-Galerking scheme (Selmin, 1987) called TTG4A, while the diffusive part is solved using a second order Galerking scheme (Donea and Huerta, 2003). TTG4A, in its cell-vertex formulation, has the advantage of having a high spectral resolution as well as moderate numerical dissipation and dispersion (Lamarque, 2007). It provides third order accuracy in space and fourth order accuracy in time (Colin and Rudgyard, 2000). It is designed for LES on hybrid meshes and has been validated in the context of turbomachinery flow applications (Collado-Morata et al., 2012, Duchaine et al., 2013, Segui et al., 2017, Odier et al., 2021). Its explicit nature brings however limitations on the characteristic cell size near the walls and the time step to ensure the acoustic CFL condition (0.9 in the present computations). In terms of subgrid scale turbulent closure, the wall-adapting local eddy viscosity (WALE) subgrid scale model of Nicoud and Ducros (1999) is used.

Simulations are run on a domain that includes a section of two blades of the SPLEEN linear high-speed low-pressure turbine cascade, as shown on Figure 2. The large dimensions of the domain in the pitchwise and spanwise directions (two pitches) are chosen to accomodate for the large turbulent structures measured in the experiments (see paragraph on turbulence generation) while applying periodicity in these directions. As said before, for case B, the domain is split in two sub-domains: a moving domain including the upstream moving bars, and a static domain containing the blades.

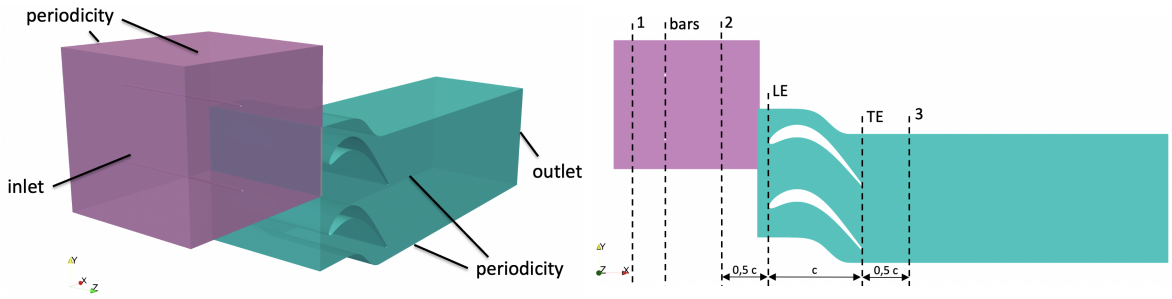

Figure 2: Sketch of the domain for case B: 3D view on the left - meridional cut on the right.

For the grid, a hybrid mesh is generated to ease the wall-resolved simulation context. Tetrahedras are used in the far field with enough resolution to accurately capture the turbulent structures induced by the bars wakes. Layers of 5 prisms and 6 prisms, for the blades and the bars respectively, are added in the boundary layers to allow the viscous sublayer resolution. This indeed allows to handle such a requirement without having a large increase in the cells number. In that respect, note that the maximal dimensionless cell size at the walls, y^+, is enforced to remain below 5 (Fig. 3). Likewise the prisms aspect ratio at walls ($\Delta x = \Delta z = \alpha \Delta y$) is controlled so that x^+ and z^+ are below 18 for the bars and below 12 on the blades. Figure 4 presents local views of the obtained mesh.

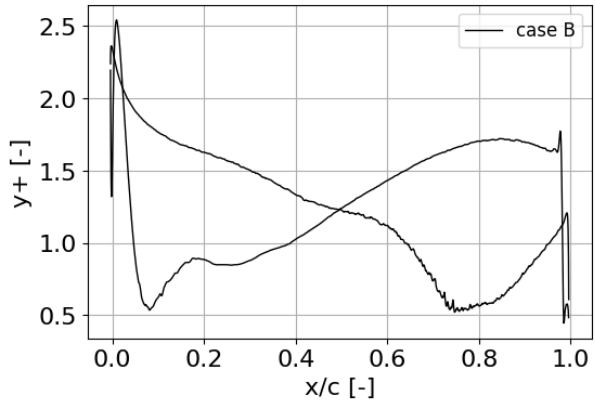

Figure 3: Dimensionless cell size on the blades for case B.

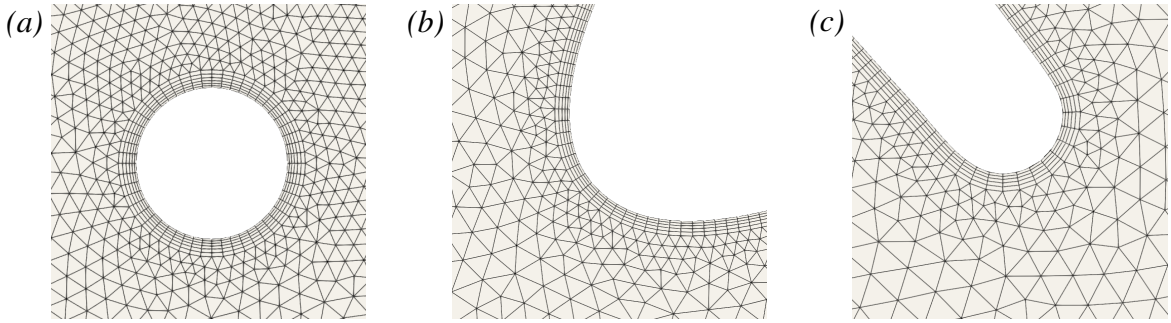

Figure 4: Views of the mesh around the bars *(a)*, the leading edges *(b)* and the trailing edges *(c)* of the blades.

The numerical setups for both cases are in all point identical. The only difference is that case A keeps only the static domain attached to the blades and the latter is slightly extended in the upstream direction so that no potential effects of the blades are visible at the inlet in order to impose a uniform total pressure field. The mesh resolutions are similar, leading to 191 million elements for case A and 322 million elements for case B.

The operating condition addressed corresponds to a blade outlet isentropic Mach number $M_{is,3}$ and an outlet isentropic Reynolds number (based on the chord length) $Re_{is,3}$ of 0.9 and 70000 respectively. With the indices corresponding to the plane number (Fig.2) where the

variable is measured, these two parameters are defined as:

$$M_{is,3} = \sqrt{\left[\left(\frac{P_{t,2}}{P_3}\right)^{(\gamma-1)/\gamma} - 1\right]\frac{2}{\gamma-1}}\,; \qquad Re_{is,3} = \frac{\rho_{is,3} V_{is,3} c}{\mu_{is,3}} \tag{1}$$

with

$$\rho_{is,3} = \frac{P_3}{RT_{is,3}},\; V_{is,3} = M_{is,3}\sqrt{\gamma R T_{is,3}},\; T_{is,3} = \frac{T_{t,2}}{1 + [(\gamma-1)/2]M_{is,3}^2} \tag{2}$$

and the dynamic viscosity defined by Sutherland's law:

$$\mu_{is,3} = \mu_{ref}\left(\frac{T_{is,3}}{T_{ref}}\right)^{3/2}\frac{T_{ref}+S}{T_{is,3}+S}\,; \tag{3}$$

$$\mu_{ref} = 1.715e\text{-}05\ [\text{Pa.s}],\ T_{ref} = 273.15\ [\text{K}] \text{ and } S = 110.4\ [\text{K}]. \tag{4}$$

In the simulations, this operating point is controlled by four parameters, the total pressure $P_{t,in}$, the total temperature $T_{t,in}$ as well as the angle of incidence α_{in} at inlet and the static pressure P_{out} at outlet. These values are imposed using the Navier-Stokes Characteristic Boundary Condition (NSCBC) formalism (Poinsot and Lele, 1992, Odier et al., 2019). An adiabatic no-slip condition is applied on the bars and blades surface. Due to the effect of the translating bars on the flow, two different sets of boundary conditions are used to keep the isentropic Reynolds number and the isentropic Mach number as close as possible for the two cases. Table 1 provides the imposed boundary conditions of the simulations as well as the resulting operating points.

	$P_{t,in}$ [Pa]	$T_{t,in}$ [K]	α_{in} [°]	P_{out} [Pa]	$Re_{is,3}$ [-]	$M_{is,3}$ [-]
case A: isolated blades	8878	285	37.3	5249	69693	0.902
case B: blades + bars	10263	302.6	37.3	5920	71617	0.900

Table 1: Summary of the boundary conditions and resulting operating points.

Note that the flow incidence at the blades leading edges may differ in both cases. Because of the presence of the upstream moving bars, the angle of attack for the blades is likely to be modified. As a matter of fact, although the incidence at the leading edges of the isolated blades is $37.3°$, it drops to $31.6°$ when upstream moving bars are present. Despite such an effect, experiments and the computations show similar loading variations on the blades with these two different angles of attack.

As discussed in the introduction, the free-stream turbulence (FST) is known to play an important role in the general flow aerodynamics, particularly impacting the boundary layer transition on the blades. Obtaining the required characteristics with accuracy is thus a crucial aspect of the computations. In all simulations discussed thereafter, synthetic turbulence is injected trough the inlet plane using the method of Bailly et al. (2002) which itself derives from the method developed by Kraichnan (1970). To comply with the experimental conditions (Simonassi et al., 2022), measured data such as the integral length scale of the turbulence (12.05 mm) and its intensity (2.34%) are imposed in both cases. The turbulent spectrum used for the injection is the Passot-Pouquet spectrum (Lepage, 2012). Also note that to account for these very large turbulent structures while imposing periodicity in the pitchwise and spanwise directions, the dimensions of the domain had to be increased to cover two pitches (65.90 mm) in both transverse directions.

The Reynolds number and Mach number conditions ($Re_{is} = 70000,\ M_{is} = 0.9$) allow to keep the CPU cost quite low. For these simulations, the convective time is defined as the time required for the flow to travel from plane 1 to plane 3 of Figure 2 and corresponds to roughly six bars passages. The transient phase of the computations (before data acquisition for the temporal averages) for both cases is about 8 convective times and the time averages are done over 10 convective times. Note that one convective time represents about 15000 CPU hours for the isolated blades and 30000 CPU hours for the case with bars (on AMD EPYC Milan 7763 - 2.45 GHz).

RESULTS AND DISCUSSION

The following section presents flow features obtained from both simulations. To do so, the operating point of the isolated blades is first validated and compared to the experiments (Simonassi et al., 2022, Lopes et al., 2022). Then the case with upstream moving bars is compared to the first one.

As shown by Medic and Sharma (2012), FST can trigger early boundary layers transition and completely modify the general blades aerodynamics. It is thus crucial to study first the flow upstream of the cascade. To do so, multiple probes have been placed in the simulations to register the temporal evolution of flow variables. Among others, a dozen of probes have been placed in the plane aligned with the blades leading edges. Probes have also been placed in plane 2 (Fig. 2) to measure velocity fluctuations upstream of the leading edges. These last probes are used to ensure that the injected synthetic turbulence characteristics comply with those measured experimentally (Simonassi et al., 2022).

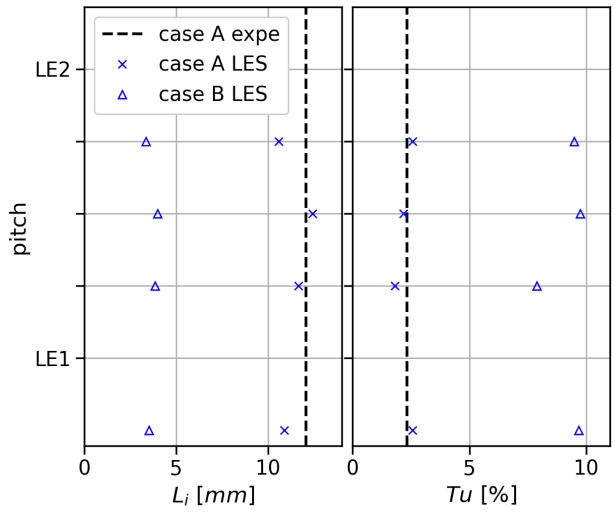

Figure 5: Characteristics (left: integral length scale, right: turbulence intensity) of the turbulence measured in experiment (black) and measured in the LES at the plane aligned with the leading edges (blue). *LE1* and *LE2* are the positions of two consecutive leading edges.

As can be seen on Figure 5, the FST at the leading edge plane for case A (without bar) is in good agreement with the experiments: i.e. $L_i = 12.05$ mm, $Tu = 2.34\%$. Note that the reported integral length scale is here obtained thanks to the autocorrelation functions of the velocity temporal evolution at each probe while the turbulence intensity follows $Tu = u_{rms}/\|V_{in}\|$, where u_{rms} corresponds to the standard deviation of the velocity signal returned by the probe

and $\|V_{in}\|$ is the velocity magnitude at inlet. Note that the obtained characteristics, measured numerically at the leading edges plane, were found to be similar at plane 2 for case A (same integral length scale and same intensity) because the characteristic time scale of the turbulence is much larger than the convective time of the flow. With the bars, the size and intensity of the eddies however differ from case A. The characteristic length is divided by approximately 3 while the intensity is nearly multiplied by 4 (Fig. 5). The bars therefore induce a change in the turbulent Reynolds number, 4/3 larger in case B comparatively to case A.

The blade loading deserves a dedicated attention since it accounts for the blade ability to generate lift, and thus power. Indeed, it is intrinsically related to the flow conditions for a given operating point knowing that the isentropic Reynolds number and isentropic Mach number are well respected as presented in Table 1. The distributions of isentropic Mach number around the blade (Fig. 6) are in fair agreement with the experimental results obtained at the Von Karman Institue for both cases (Lopes et al., 2022). However, a difference is noticeable on the pressure side. Figure 7 shows the presence of recirculation bubbles on the pressure and suction sides of the blades in the mean velocity field of case A. Following the distribution of isentropic Mach number retrieved experimentally, the separation on the pressure side seems to be shorter in the experiment. A lack of turbulence in the boundary layers can be the origin of the separation observed in the LES. Further computations with laminar inlet flow indeed showed that the FST injected here ($L_i = 12.05$ mm, $Tu = 2.34\%$) has no influence on the boundary layers behaviour. The very large size of the turbulent structure injected at the inlet conjugated with the injection method could explain this result although more investigations appear needed. Note also that the considered Passot-Pouquet spectrum lacks of small structures (Lepage, 2012) that could interact with the boundary layers and provoke an earlier transition of the latter.

Comparatively, case B presents a lower loading due to the average flow reduction of incidence induced by the bars wakes. This results in a reduction of isentropic Mach number on the first part of the suction side and, on the other hand, an increase of isentropic Mach number on the pressure side near the leading edge.

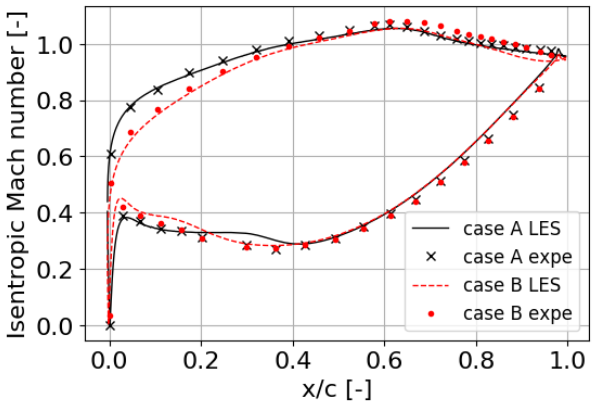

Figure 6: Loading on the blades for case A (black) and case B (red).

In contrast to case A, case B presents an unsteady aerodynamics due to the periodically incoming wakes. The events sequence occurring during a period of blade passage is presented in the following. Figure 8 presents phase averages of case B for different positions of the bars with respect to the blades. The averages are computed based on 36 bars passages (36 snapshots) which corresponds to approximately 6 convective times. 5 phases are presented here, from *(a)*

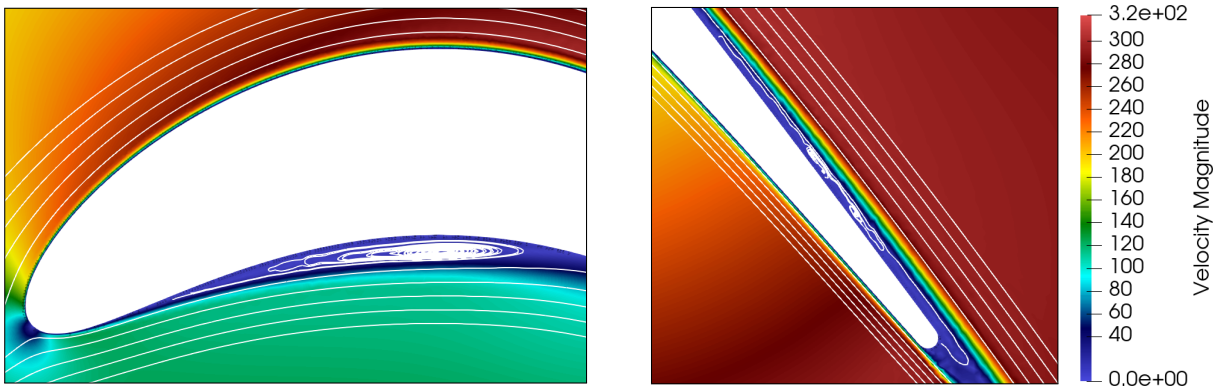

Figure 7: Mean velocity field and streamlines for case A showing recirculation bubbles on the pressure side (left) and the suction side (right).

to *(e)* in Figure 8 where phase *(a)* corresponds to the time at which the wakes reach the blades leading edges.

When the wakes are aligned with the blades leading edges (item I in phase *(a)*), the flow incidence at the LE is reduced due to the wakes. This leads to a reduction of Mach number on the first part of the suction side and an enlargement of the recirculation bubble on the pressure side (visible on the right in phase *(a)* of Fig. 8). This low velocity pocket is then convected downstream on the pressure side during the period between two passages of consecutive wakes (item II in phase *(d)*). On the suction side, an acceleration of the flow generates a sonic pocket (item III in phase *(a)*) which is then convected downstream along the blade surface. This acceleration due to the wake is explained by Hodson and Howell (2005b) as the wake can be thought of as a "negative" jet flowing towards the wake origin superimposed to a uniform freestream. In the vicinity of the suction side, downstream of the wake center, the perturbation from the negative jet accelerates the flow, while upstream of the wake center, the perturbation decelerates the flow. A sonic region precedes the wake segment in the inter-blade channel due to this acceleration. The turbulent kinetic energy fields presented in Figure 8 are also in agreement with the observations of Hodson and Howell (2005b). The wake segment is bowed in the bladerow near the leading edge plane where the mid-passage velocities are higher than the velocities near the blade surfaces (item IV in phase *(d)*). It is then accelerated over the suction surface of the blade, thus increasing the wake width in that region.

The boundary layer on the suction side remains globally attached for case B (Fig.9). However a thin recirculation bubble remains visible in Figure 10, corresponding to a zoom on the suction side at phase *(c)* (item V). The separation is located in the downstream part of the sonic pocket moving in the bladerow and is present in phases *(c)* and *(d)*. Afterwards, the turbulent wake segment present in this zone in phase *(d)* triggers the transition (visible in the TKE field on Fig. 8) and reattachment of the boundary layer (item VI in phase *(e)*), leading to an increase of the wall shear stress near the trailing edges of the blades (item VII in phase *(e)*).

The pressure losses are also affected by the wakes passage. Figure 11 shows oscillations of total pressure at the frequency of the bars at plane 3 for case B while the latter is nearly constant for case A. The difference of mean total pressure at plane 3 between the two cases is due to their slightly different operating conditions (Tab. 1). Losses have been separately evaluated for each case. The mean total pressure losses between plane 2 and plane 3 (Fig. 2) are 1.5 times higher for case B (with bars) than for case A. One hypothesis is that it could be explained by the off-

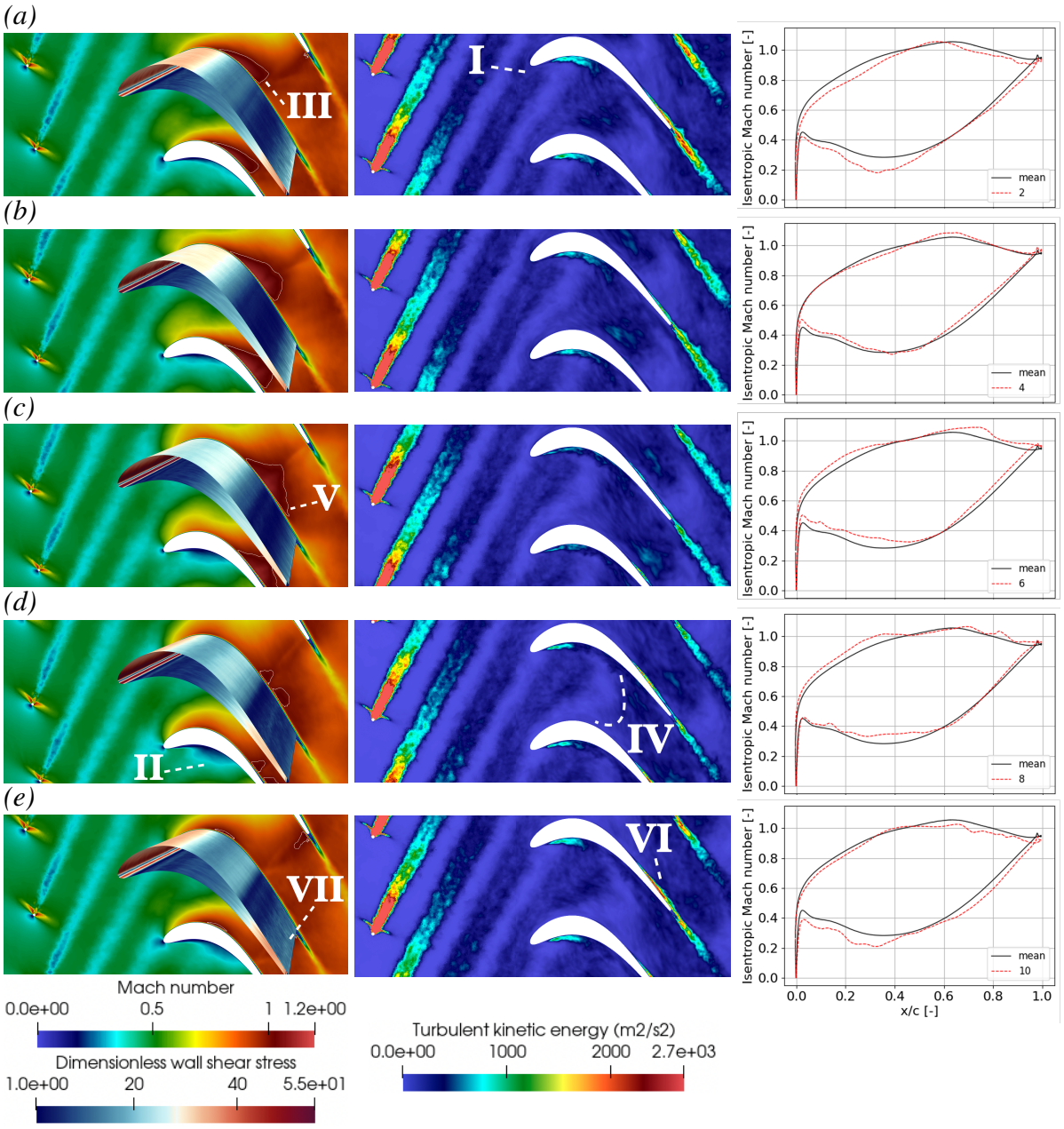

Figure 8: Phase averages of case B for different positions of the bars with respect to the blades. Left: Mach number field with isocontour $M = 1$ (white) and dimensionless wall shear stress on the blade surface. Center: turbulent kinetic energy field. Right: distributions of isentropic Mach number in comparison with the mean distribution of case B.

design operation of the blades due to the wakes, mainly the sub-incidence of the flow coming at the leading edges. However the share between the influence of the wakes and the influence of the sub-incidence cannot be done. Further iterations on this configuration should be conducted to find the correct boundary conditions to obtain the same incidence with and without upstream bars.

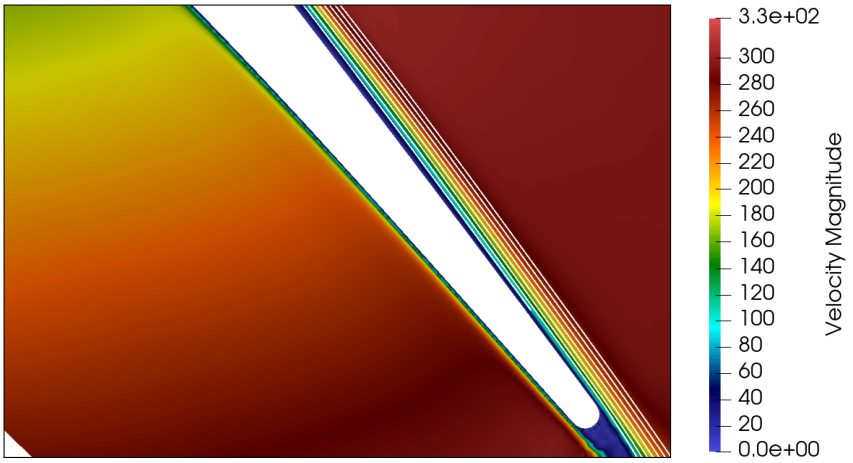

Figure 9: Mean velocity field and streamlines on the suction side for case B.

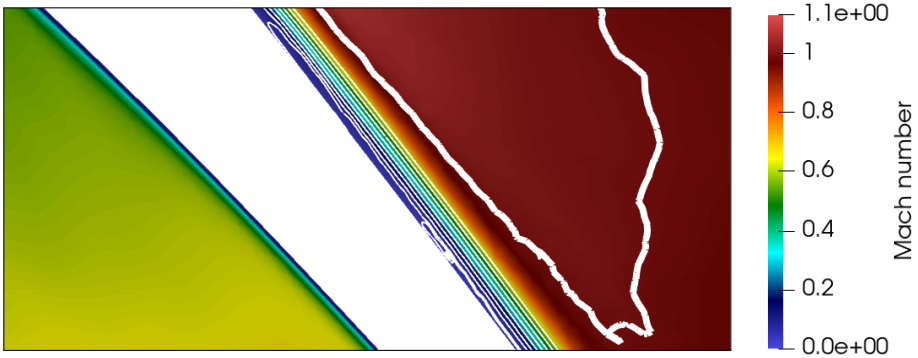

Figure 10: Zoom on the suction side for case B in phase *(c)* (item V): Mach number field with streamlines (thin white) and isocontour $M = 1$ (thick white).

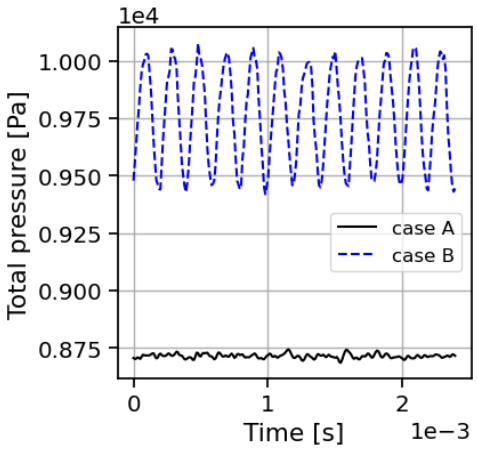

Figure 11: Temporal evolution of the total pressure at plane 3. Note that the difference of mean total pressure is due to the difference of operating point between the two cases.

CONCLUSIONS

A new generation of low-pressure turbine is nowadays designed for the future architectures of aeronautical engines. These high-speed LPT have the particularity of having locally transonic flow regime due to their higher rotation rate. The aerodynamic mechanisms of such high Mach operating conditions of LPT are not well known yet. The code AVBP (Schonfeld and Rudgyard, 1999) showed its ability to tackle this configuration by use of Large-Eddy Simulations.

Two cases were investigated within this study: a first one composed of a blades cascade operating at nominal conditions and a second one where upstream moving bars, acting as wake generators, are added. The reference case (without upstream moving bars) was validated compared to experimental results and showed good agreement for the isentropic Mach number distribution along the blade, as well as the Reynolds number and Mach number. The full configuration, with upstream moving bars, was then studied to evaluate the impact of the periodically incoming wakes on such transonic blades.

Considering the flow upstream of the blades, it is shown that the presence of wakes in the incoming flow reduces the characteristic size of the turbulence while producing a more intense fluctuating field. At the leading edges of the blades, the incidence of the flow is reduced by the wakes, going from $37.3°$ for reference conditions to $31.6°$ when bars are present. It has an impact on the loading of the blades visible on the distribution of isentropic Mach number on the blades surface. In the inter-vane channels, the wakes are segmented and bowed due to the mean velocity gradients. These turbulent wake segments cause local accelerations and decelerations of the flow leading to sonic pockets on the suction sides and trigger the transition of the boundary layers.

ACKNOWLEDGEMENTS

This work was granted access to the HPC resources of CCRT (Centre de Calcul Recherche et Technologie). The authors also acknowledge Safran Aircraft Engines for providing the geometry used in the computations and their follow-up trough the study. A last thanks to the Von Karman Institute who provided the experimental results for the comparisons.

REFERENCES

C. Bailly, X. Gloerfelt, and C. Bogey. Report on stochastic noise source modelling. Technical report, École Centrale de Lyon, 2002.

P. Bechlars, R. Pichler, and R. D. Sandberg. Characterisation of the turbulence-separation-bubble interaction on turbine blades. In *20th Australasian Fluid Mechanics Conference*, Perth, Australia, 2016.

M. Bolinches-Gisbert, D. C. Robles, R. Corral, and F. Gisbert. Numerical and experimental investigation of the reynolds number and reduced frequency effects on low-pressure turbine airfoils. *Journal of Turbomachinery*, 143, 2 2021.

O. Colin and M. Rudgyard. Development of high-order taylor-galerkin schemes for LES. *Journal of Computational Physics*, 162:338–371, 2000.

E. Collado-Morata, N. Gourdain, F. Duchaine, and L. Y. Gicquel. Effects of free-stream tur-

bulence on high pressure turbine blade heat transfer predicted by structured and unstructured LES. *International Journal of Heat and Mass Transfer*, 55:5754–5768, 2012.

J. de Laborderie, F. Duchaine, L. Gicquel, O. Vermorel, G. Wang, and S. Moreau. Numerical analysis of a high-order unstructured overset grid method for compressible LES of turbomachinery. *Journal of Computational Physics*, 363:371–398, 2018.

J. de Laborderie, F. Duchaine, L. Gicquel, and S. Moreau. Wall-modeled Large-Eddy simulations of a multistage high-pressure compressor. *Flow, Turbulence and Combustion*, 104: 725–751, 2020.

J. Dombard, F. Duchaine, L. Gicquel, N. Odier, K. Leroy, N. Buffaz, S. Le-Guyader, J. Démolis, S. Richard, and T. Grosnickel. Evaluation of the capacity of RANS/URANS/LES in predicting the aerodynamic performance of a state-of-the-art high-pressure turbine-effect of load and off design operation. In *ASME Turbo Expo*, London, United-Kingdom, 2020.

J. Donea and A. Huerta. *Finite element methods for flow problems*. Wiley, 2003.

F. Duchaine, N. Maheu, V. Moureau, G. Balarac, and S. Moreau. Large eddy simulation and conjugate heat transfer around a low-mach turbine blade. *Journal of Turbomachinery*, 136 (5), 2013.

D. Dupuy, L. Gicquel, N. Odier, F. Duchaine, and T. Arts. Analysis of the effect of intermittency in a high-pressure turbine blade. *Physics of Fluids*, 32, 2020.

H. P. Hodson and R. J. Howell. The role of transition in high-lift low-pressure turbines for aeroengines. *Progress in Aerospace Sciences*, 41:419–454, 2005a.

H. P. Hodson and R. J. Howell. Bladerow interactions, transition, and high-lift aerofoils in low-pressure turbines. *Annual Review of Fluid Mechanics*, 37:71–98, 2005b.

R. H. Kraichnan. Diffusion by a random velocity field. *Physics of Fluids*, 13:22–31, 1970.

N. Lamarque. *Schémas numériques et conditions limites pour la simulation aux grandes échelles de la combustion diphasique dans les foyers d'hélicoptère*. PhD thesis, Institut National Polytechnique de Toulouse, 2007.

P. Lepage. *Implémentation de la technique de simulation des grandes échelles dans un solveur parallèle de dynamique des fluides*. PhD thesis, Université de Sherbrooke, 2012.

G. Lopes, L. Simonassi, A. Torre, M. Patinios, and S. Lavagnoli. An experimental test case for transonic low-pressure turbines - part 2: Cascade aerodynamics at on- and off-design reynolds and mach numbers. In *ASME Turbo Expo*, Rotterdam, The Netherlands, 2022.

X. Lu, Y. Zhang, W. Li, S. Hu, and J. Zhu. Effects of periodic wakes on boundary layer development on an ultra-high-lift low pressure turbine airfoil. *Proceedings of the Institution of Mechanical Engineers, Part A: Journal of Power and Energy*, 231:25–38, 2017.

G. Medic and O. Sharma. Large-Eddy simulation of flow in a low-pressure turbine cascade. In *ASME Turbo Expo*, Copenhagen, Denmark, 2012.

V. Michelassi, J. Wissink, and W. Rodi. LES of flow in a low pressure turbine with incoming wakes. *High Performance Computing in Science and Engineering*, 02:335–346, 2003a.

V. Michelassi, J. G. Wissink, and W. Rodi. Direct numerical simulation, large eddy simulation and unsteady reynolds-averaged navier-stokes simulations of periodic unsteady flow in a low-pressure turbine cascade: A comparison. *Proceedings of the Institution of Mechanical Engineers, Part A: Journal of Power and Energy*, 217:403–412, 2003b.

V. Michelassi, L. W. Chen, R. Pichler, and R. D. Sandberg. Compressible direct numerical simulation of low-pressure turbines-part ii: Effect of inflow disturbances. *Journal of Turbomachinery*, 137, 2015.

F. Nicoud and F. Ducros. Subgrid-scale stress modelling based on the square of the velocity gradient tensor. *Flow, Turbulence and Combustion*, 62:183–200, 1999.

N. Odier, T. Poinsot, F. Duchaine, L. Gicquel, and S. Moreau. Inlet and outlet characteristics boundary conditions for large eddy simulations of turbomachinery. In *Proceedings of the ASME Turbo Expo 2019: Turbomachinery Technical Conference and Exposition*, volume 2 C, pages 1–11, Phoenix, USA, 6 2019. ASME.

N. Odier, A. Thacker, M. Harnieh, G. Staffelbach, L. Gicquel, F. Duchaine, N. G. Rosa, and J. D. Müller. A mesh adaptation strategy for complex wall-modeled turbomachinery LES. *Computers and Fluids*, 214, 2021.

T. J. Poinsot and S. K. Lele. Boundary conditions for direct simulations of compressible viscous flows. *Journal of Computational Physics*, 101:104–129, 1992.

T. Schonfeld and M. Rudgyard. Steady and unsteady flow simulations using the hybrid flow solver AVBP. *AIAA journal*, 37:1378–1385, 1999.

L. M. Segui, L. Y. M. Gicquel, F. Duchaine, and J. D. Laborderie. LES of the LS89 cascade: influence of inflow turbulence on the flow predictions. In *12th European Conference on Turbomachinery Fluid dynamics & Thermodynamics*, Stockholm, Sweden, 2017.

V. Selmin. Third-order finite element schemes for the solution of hyperbolic problems. Technical report, Institut National de Recherche en Informaique et en Automatique, 1987.

L. Simonassi, G. Lopes, S. Gendebien, A. Torre, M. Patinios, S. Lavagnoli, N. Zeller, and L. Pintat. An experimental test case for transonic low-pressure turbines - part 1: Rig design, instrumentation and experimental methodology. In *ASME Turbo Expo*, Rotterdam, The Netherlands, 2022.

G. Wang, F. Duchaine, D. Papadogiannis, I. Duran, S. Moreau, and L. Y. Gicquel. An overset grid method for large eddy simulation of turbomachinery stages. *Journal of Computational Physics*, 274:333–355, 2014.